Research Article Vol. 34, No. 7 / 6 Apr 2026 / Optics Express 11847

Optics EXPRESS

Characterization of source coherence requirements for laboratory x-ray diffraction imaging

SUNGHOON CHOI, SORA PARK, JUN-TAE KANG, AND JIN-WOO JEONG*

Materials and Components Research Division, Electronics and Telecommunications Research Institute (ETRI), 218 Gajeong-ro, Daejeon 34129, Republic of Korea
*jinu@etri.re.kr

Abstract: Young's double-slit (YDS) fringe visibility provides a detector-accessible measure of spatial coherence, but implementing hard-X-ray YDS experiments with compact laboratory sources is fundamentally constrained by the coherence–flux trade-off imposed by spatial filtering. Here we present an end-to-end simulation framework that couples SHADOW3 ray statistics with WOFRY wave-optics propagation to evaluate detector-level interference patterns and feasibility metrics under partial coherence. Partial coherence is defined directly at the pinhole plane by discretizing the pinhole-filtered angular spectrum into a weighted angular-tilt ensemble, which is propagated through Fresnel (pinhole to slit) and Fraunhofer (slit to detector) operators with energy-conserving binning onto an oversampled detector grid. Across parameter sweeps of effective source size w (20–200 µm), source–pinhole distance S (3.0–4.7 m), pinhole diameter D (3–10 µm), pinhole–slit distance R (0.01–1.0 m), and Gaussian relative bandwidth σ_{BW} (0.1–5%), we evaluate Michelson visibility V, detector-ROI photon counts N_{det}, and a photon-statistics-aware figure of merit $FOM = V^2 N_{det}$. To capture bandwidth-driven degradation not reflected by global visibility alone, we additionally introduce a longitudinal-coherence wash-out metric LC_{ratio}. The resulting inverse-design maps reveal two distinct operating regimes. For larger sources ($w\sim200$ µm), the feasible design space becomes visibility-limited, while smaller sources ($w\sim50$ µm) operate primarily in a throughput-limited regime where performance improves monotonically with photon acceptance. Absolute photon statistics are anchored by calibrating the pinhole-transmitted flux to a published laboratory benchmark ($\approx 5 \times 10^3$ ph/s through a 5 µm pinhole at 0.1% σ_{BW}), enabling exposure-time interpretation of the design maps in experimentally meaningful units. The framework therefore provides a quantitative guideline for selecting source filtering and propagation geometry in compact laboratory YDS measurements under realistic coherence and photon-statistics constraints.

1. Introduction

Young's double-slit (YDS) fringe visibility provides a direct measure of spatial coherence because the interference contrast is governed by the mutual coherence between the two slit positions. The concept of optical coherence dates to Zernike's formal definition of the degree of coherence in 1938, building on Young's foundational interference experiment in the nineteenth century [1,2].

Hard-X-ray YDS experiments were demonstrated much later. Kohn et al. related fringe visibility to transverse coherence length in synchrotron radiation [3], while Leitenberger et al. observed interference fringes in the 8–19 keV range and quantified the reduction of fringe contrast with increasing effective source size [4]. These early demonstrations were primarily conducted at third-generation synchrotron facilities, where long beamlines and high coherent flux make high-contrast fringe measurements comparatively accessible [5,6].

#586471
Journal © 2026

https://doi.org/10.1364/OE.586471
Received 3 Dec 2025; revised 5 Mar 2026; accepted 8 Mar 2026; published 24 Mar 2026

Compact laboratory X-ray sources represent a potentially transformative alternative, but they typically offer substantially lower spatial coherence than synchrotron beams. Recent studies using gallium liquid-metal-jet (LMJ) sources have demonstrated the feasibility of YDS measurements in laboratory conditions [7]. Practical deployment, however, is constrained by a fundamental coherence–flux trade-off: achieving sufficient transverse coherence in a compact geometry typically requires strong spatial filtering (e.g., pinholes/apertures), which reduces photon throughput and can drive long exposure times. These limitations become particularly restrictive in demanding use cases such as coherent diffraction imaging (CDI) of thick specimens, where usable fringe visibility and transmission must be satisfied within realistic acquisition times [8,9].

The objective of this work is to quantify the minimum spatial and temporal coherence requirements needed for a laboratory source to produce discernible Young's fringes in a compact, hard-X-ray YDS geometry, while explicitly accounting for detector sampling constraints and photon statistics.

To this end, we present an end-to-end workflow that couples SHADOW3-derived ray statistics with WOFRY wave-optics propagation to produce detector-level feasibility and inverse-design maps under partial coherence. The key methodological choice is that partial coherence is defined directly at the pinhole plane, using the pinhole-filtered angular spectrum. This avoids ambiguity in coherence transformations introduced by upstream focusing optics, while remaining compatible with benchmark-anchored flux normalization based on published laboratory conditions [7]. Quantitative performance is reported using conventional Michelson visibility, detector-region photon budgets, and a longitudinal-coherence washout criterion designed to capture bandwidth-driven outer-fringe suppression.

2. Simulation framework

2.1. Hybrid SHADOW3-WOFRY workflow

All simulations were performed using OASYS, coupling SHADOW3 for Monte Carlo ray tracing with WOFRY for scalar wave-optics propagation [10,11]. SHADOW3 provides ray phase-space statistics (positions and direction cosines) for an extended laboratory source, while WOFRY propagates complex wavefronts through the pinhole and double slit using Fresnel and Fraunhofer operators [12]. The hybrid approach enables detector-level modeling of partially coherent diffraction patterns using a numerically constructed ensemble of coherent realizations.

We adopt the coordinate convention consistent with the SHADOW3 ray output used in the workflow: the optical axis coincides with the beam propagation direction (y), and the transverse coordinates in each plane are (x, z). For each ray transmitted through the pinhole, the paraxial angles at the pinhole plane are computed from direction cosines v_x, v_y, v_z as:

$$\theta_x \approx \frac{v_x}{v_y},\ \theta_z \approx \frac{v_z}{v_y}, \tag{1}$$

These pinhole-transmitted rays define a two-dimensional angular histogram $p(\theta_x,\ \theta_z)$, which is subsequently discretized into a finite set of tilt modes and weights for the partial-coherence ensemble.

Figure 1 illustrates the definition of the angular spectrum used to construct the partial-coherence ensemble. The pinhole acts as a spatial filter that selects a subset of rays from the extended source. The transmitted rays define the effective angular spread at the pinhole plane, which serves as the reference plane for coherence modeling. By defining coherence at this plane, the method avoids ambiguity associated with magnification or divergence changes introduced by upstream optical elements. Each tilt mode represents one coherent realization; the detector intensity is obtained by incoherent averaging with SHADOW3-derived weights.

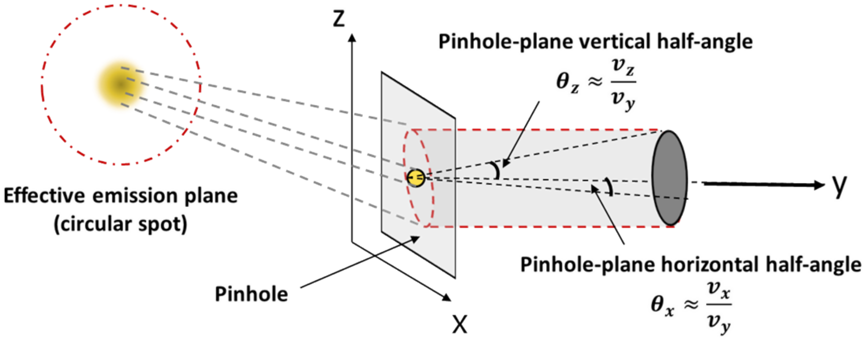

Fig. 1. Definition of the angular spectrum at the pinhole plane. The effective emission plane represents the source including any upstream focusing optics (if present). Rays transmitted through the pinhole define the angular spread (half-angles θ_x, θ_z), which is used to construct the partial-coherence ensemble. Coherence is defined at the pinhole plane and is independent of upstream focusing elements.

2.2. Simulation geometry and propagation models

The full simulation geometry is shown in Fig. 2. A circular pinhole of diameter (D) is located a distance (S) downstream of the effective emission plane. The pinhole acts as a spatial filter that improves transverse coherence at the slit plane at the expense of flux. The pinhole-transmitted field is propagated a distance (R) to the double-slit plane using Fresnel diffraction. The diffracted field from the double slit is propagated a distance (L) to the detector using a Fraunhofer operator [13].

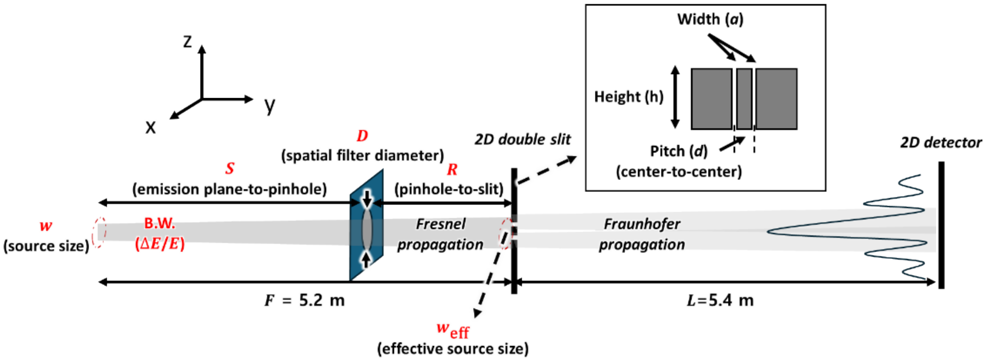

Fig. 2. OASYS simulation geometry: a partially coherent laboratory X-ray source, a pinhole aperture as a spatial filter, Fresnel propagation to the double-slit plane, and Fraunhofer propagation to a two-dimensional detector.

The double-slit aperture is characterized by slit width (a), center-to-center separation (d), and slit height (h). The expected far-field fringe period is:

$$\Lambda = \frac{\lambda L}{d}, \tag{2}$$

which defines the detector sampling criterion. Simulations are performed with ≥20 pixels per fringe period to ensure that visibility degradation reflects physical coherence effects rather than numerical undersampling [14].

Detector sampling is treated as an explicit design constraint. The far-field intensity is first computed on a high-resolution internal grid (optionally with FFT zero-padding to increase sampling density) and then mapped to detector pixels by energy-conserving (area-integrated) binning, i.e., integrating intensity over each pixel area so that total photon flux is preserved under downsampling.

2.3. Spatial coherence modeling via an angular-tilt ensemble

Within WOFRY's wave-optics framework, the built-in SHADOW3Wavefront reconstruction (within the *shadow3_wavefront* module) yields a single coherent field and implicitly assumes that all rays belong to one mutually coherent beam [15]. This is not adequate for an extended laboratory source with finite angular divergence. We therefore model transverse partial coherence explicitly by constructing a weighted angular-tilt ensemble derived from the pinhole-filtered angular spectrum in Fig. 1.

Let $U_0(X, Z)$ denote the complex field immediately downstream of the pinhole. A coherent ensemble member with angular tilt $(\theta_x^{(m)}|\theta_z^{(m)})$ is represented as:

$$U^{(m)}(X, Z) = U_0(X, Z) \exp[ik(\theta_x^{(m)} X + \theta_z^{(m)} Z)], \tag{3}$$

where $k = 2\pi/\lambda$. The tilt angles and weights (w_m) are extracted from the discretized pinhole-plane angular histogram $p(\theta_x,\ \theta_z)$, with $\sum_{m=1}^{M} w_m = 1$.

Each ensemble member is propagated independently through the optical system. The detector intensity for photon energy (E) is obtained as an incoherent weighted sum:

$$I_{det}(x, z; R, E) = \sum_{m=1}^{M} w_m |H_L\{O \cdot F_R[U^{(m)}(X, Z)]\}|^2, \tag{4}$$

where F_R denotes Fresnel propagation from the pinhole to the slit plane over distance R, $O(X,\ Z)$ is the double-slit transmission function, and H_L denotes Fraunhofer propagation to the detector over distance L. Increasing the angular width of the pinhole-filtered distribution reduces mutual coherence at a fixed slit separation, consistent with the qualitative scaling described by Pieter van Cittert and Zernike [1,16].

To quantify transverse coherence directly at the slits, we compute the complex degree of coherence $(|\gamma_{12}|)$ from slit-integrated complex amplitudes (definitions and usage are provided in the Quantitative analysis section). This construction provides a direct wave-optics realization of transverse partial coherence.

2.4. Temporal coherence modeling

Finite spectral bandwidth limits longitudinal coherence and can suppress fringes away from the central peak. We model temporal coherence by sampling a normalized spectral density $S(E)$ (Gaussian line centered at E_0):

$$\int S(E) dE = 1. \tag{5}$$

The spectrum is discretized into N energy samples (E_k) (in this work N=21, spanning ±3σ), and the polychromatic detector intensity is computed as:

$$I_{poly}(x, z) = \sum_{k=1}^{N=21} w_k I_{det}(x, z; R, E_k). \tag{6}$$

2.5. Practical feasibility and flux normalization

Because a micron-scale pinhole significantly reduces flux, realistic photon statistics are enforced through detector-level flux normalization. Following the benchmark strategy used in [7], the pinhole-transmitted flux is calibrated such that a 5 μm pinhole transmits approximately 5×10^3 photons/s at 0.1% (Gaussian σ) bandwidth under the benchmark source assumptions. For other bandwidths, the transmitted photon flux is scaled proportionally to $\Delta E/E$ under the same source assumptions, and propagated through the full simulation to obtain ROI-integrated detector counts.

For manufacturability discussion, absorber thicknesses in the tens-of-microns range are assumed for the double-slit mask; this enters only feasibility discussion and does not modify the scalar diffraction model of an ideal opaque aperture. In practical implementations, meter-scale propagation distances used here to simplify fringe sampling can be accompanied by vacuum or He flight paths to reduce air absorption and phase distortion.

2.6. Simulation workflow

Simulations were performed at a photon energy of 9.25 keV (Ga Kα, λ=0.134 nm). The double-slit geometry was fixed to $a = 1$ μm, $d = 2$ μm, $h = 50$ μm and the slit-to-detector distance was fixed to L=5 m, giving a fringe period $\Lambda \approx 0.335$ mm via Eq. (2). In the simulations reported here, a typical choice is 10 μm pixel pitch, which yields ∼33 pixels per fringe at the reference energy and geometry.

The multi-parameter sweep follows the loop variables implemented in the hybrid workflow and is summarized in Table 1. The key inverse-design view is a set of smooth design maps over the (R, D) plane computed for each (w, S, σ_{BW}) condition.

Table 1. Fixed and swept parameters explored in the inverse-design sweep.

Category	Parameter	Symbol	Value / Range
Fixed	Energy	E_0	9.25 keV
	Slit width	a	1 μm
	Slit pitch (center-to-center)	d	2 μm
	Slit height	h	50 μm
	Slit-to-detector distance	L	5
Swept	Source diameter (effective emission plane)	w	20–200 μm
	Source-to-pinhole distance	S	3.0, 3.9, 4.7 m
	Pinhole diameter	D	3, 5, 7, 10 μm
	Pinhole-to-slit distance	R	0.01–1.0 m
	Relative bandwidth (Gaussian σ_{BW})	$\Delta E/E$	0.1%, 1%, 2%, 5%

3. Quantitative analysis

All quantitative metrics are extracted from pixel-integrated detector data after energy-conserving binning. Unless otherwise stated, a rectangular detector region of interest (ROI) is used to evaluate photon statistics, and a horizontal centerline profile is obtained by averaging several detector rows around the optical axis. The ROI is chosen to include multiple fringe periods and to support outer-fringe evaluation required by the longitudinal-washout metric.

3.1. Michelson visibility extraction

Visibility is evaluated using the conventional Michelson definition:

$$V = \frac{I_{\max} - I_{\min}}{I_{\max} + I_{\min}}. \tag{7}$$

To reduce bias from the slowly varying single-slit diffraction envelope, the centerline intensity is detrended by estimating the envelope with a smoothing window of approximately one fringe period and dividing the centerline by this envelope prior to extracting $I_{\max}$ and $I_{\min}$. A moderate-contrast constraint (V = 0.5) is used as the operational design threshold for feasibility and inverse-design maps [17].

3.2. Photon statistics and figure of merit

Detector photon statistics are computed at the detector plane as ROI-integrated photon counts for an exposure time t_{exp}:

$$N_{\text{det}} = \Phi_{\text{ROI}}\, t_{\text{exp}}\, \text{QE}, \tag{8}$$

where Φ_{ROI} is the ROI photon flux after pixel integration and QE is detector quantum efficiency. Unless otherwise stated, QE=1 is used so that N_{det} represents incident ROI photons, enabling detector-independent comparison across geometries.

A practical inverse-design figure of merit (FOM) that couples contrast and photon statistics is defined as:

$$\text{FOM} \equiv V^2 N_{\text{det}}, \tag{9}$$

motivated by the approximate $V\sqrt{N}$ scaling of contrast estimation signal-to-noise in the photon-limited regime [18].

3.3. Slit-plane complex degree of coherence and equivalent effective source size

Transverse coherence is quantified directly at the slit plane by computing slit-integrated complex amplitudes and the complex degree of coherence. Let $A_1^{(m)}$ and $A_2^{(m)}$ denote the slit-integrated complex amplitudes for ensemble member m. The mutual intensity and slit intensities are:

$$J_{12} = \sum_m w_m A_1^{(m)} (A_2^{(m)})^*, \tag{10}$$

$$I_1 = \sum_m w_m |A_1^{(m)}|^2, I_2 = \sum_m w_m |A_2^{(m)}|^2, \tag{11}$$

and the complex degree of coherence is:

$$|\gamma_{12}| = \frac{|J_{12}|}{\sqrt{I_1 I_2}}. \tag{12}$$

For balanced illumination ($I_1 = I_2$), detector visibility is expected to track $|\gamma_{12}|$, in the ideal two-beam interference model described by Mandel and Wolf [18]. To provide an intuitive, single-parameter coherence descriptor, we additionally report a Gaussian-equivalent effective source size w_{eff} (FWHM) derived by inverting the standard Gaussian mutual-coherence form:

$$|\gamma_{12}| \approx \exp\left[-2\left(\frac{\pi\sigma_s d}{\lambda R}\right)^2\right], \tag{13}$$

$$w_{\text{eff}} = \text{FWHM} = 2\sqrt{2\ln 2}\,\sigma_s. \tag{14}$$

where σ_s is the equivalent RMS source width and d is the slit separation.

3.4. Longitudinal washout evaluation

To explicitly capture bandwidth-induced fringe washout far from the central peak, we compute a position-dependent local Michelson visibility along the detector centerline and define:

$$LC_{\text{ratio}} = \frac{V_{\text{outer}}}{V_{\text{center}}}, \tag{15}$$

where V_{center} is averaged over a central window and V_{outer} is averaged over an outer-fringe region, providing a detector-level criterion that is explicitly sensitive to far-fringe washout. This criterion complements global visibility measures by being sensitive to outer-fringe suppression that is characteristic of limited longitudinal coherence.

4. Results

4.1. Representative detector patterns and quantitative lineouts

We first examine how the primary transverse-coherence design parameters influence the diffraction–interference pattern at the detector. Because the full parameter sweep produces a large ensemble of images, Fig. 3 summarizes representative comparisons in a compact 2×2 layout. Each panel is shown as a half-split composite, where the left half corresponds to a higher-coherence condition and the right half corresponds to a lower-coherence condition. In each pair, only the labeled parameter is varied while the remaining parameters are fixed. The red vertical line indicates the split boundary ($x = 0$), and the dashed horizontal line marks the centerline ($z = 0$) used for extracting the one-dimensional profiles. All panels share the same linear color scale in expected detector counts per pixel, enabling direct comparison of fringe morphology and photon throughput.

Across the four transverse-coherence control parameters (w, S, R, and D), a consistent trend is observed: conditions that produce a smaller Gaussian-equivalent effective source size w_{eff} generate stronger fringe modulation, whereas larger w_{eff} leads to progressive contrast loss and eventual fringe washout.

In the source-size comparison [Fig. 3(a)], increasing the source diameter from w=50 µm to 200 µm increases w_{eff} (≈1.04 µm → ≈4.04 µm), and the interference fringes become visibly broadened and weakly modulated. A similar trend appears in the pinhole-diameter comparison [Fig. 3(d)]. Increasing the pinhole diameter from D=3 µm to 10 µm increases w_{eff} (≈0.96 µm → ≈4.04 µm) because the larger aperture admits a broader angular spectrum at the pinhole plane, increasing the incoherent modal content at the slits and reducing fringe visibility despite the higher photon throughput.

The pinhole-to-slit distance R provides an additional control through Fresnel propagation [Fig. 3(c)]. Reducing R from 0.10 m to 0.01 m decreases w_{eff} (≈0.96 µm → ≈0.36 µm) and restores higher-contrast fringes, indicating that near-field propagation from the pinhole significantly influences the mutual coherence at the slit separation. Finally, changing the source-to-pinhole distance S modifies the angular filtering imposed by the pinhole [Fig. 3(b)]. Increasing S narrows the transmitted angular distribution, producing a smaller w_{eff} and a sharper fringe pattern, although at the cost of reduced photon flux.

To quantitatively relate the two-dimensional patterns in Fig. 3 to the extracted interference metrics, Fig. 4 shows horizontal line profiles taken along the dashed guide in Fig. 3 ($z = 0$). Five detector rows around the optical axis are averaged to obtain a representative one-dimensional intensity profile as a function of detector coordinate x. Within each panel, the two curves are normalized by the larger peak value so that modulation depth can be compared independently of total photon throughput. The dashed black curve denotes the ideal coherent Fraunhofer double-slit reference evaluated for the same slit geometry and detector sampling.

The profiles in Fig. 4(a)–(d) confirm that the changes observed in Fig. 3 arise primarily from variations in fringe contrast rather than shifts in fringe spacing or diffraction geometry. Fringe

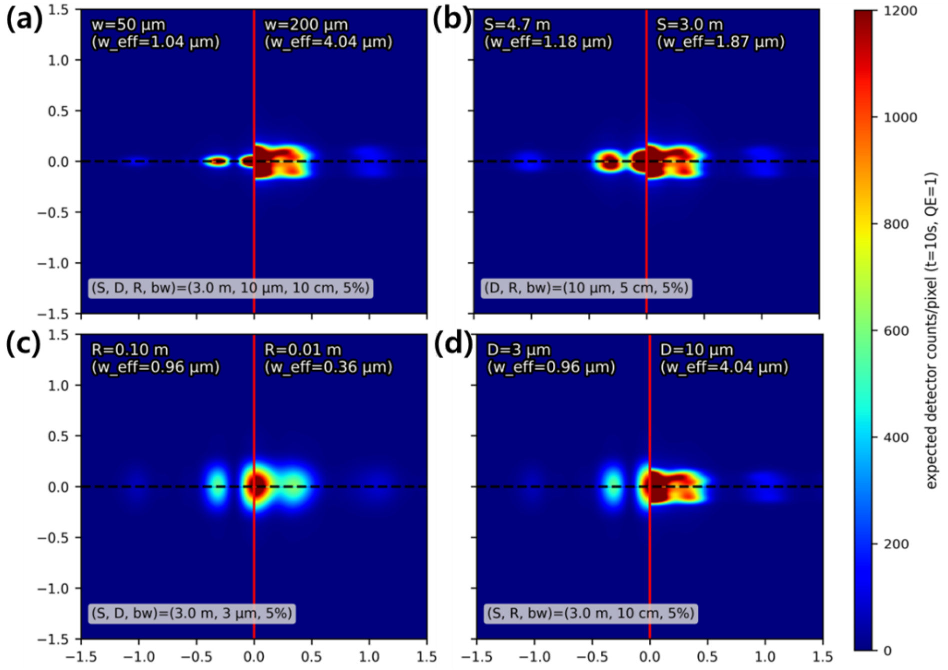

Fig. 3. Effect of transverse-coherence design parameters on the detector diffraction–interference pattern. Each panel shows a half-split comparison between higher-coherence (left) and lower-coherence (right) conditions, where only the labeled parameter is varied: (a) source size w, (b) source-to-pinhole distance S, (c) pinhole-to-slit distance R, and (d) pinhole diameter D. Smaller effective source size w_{eff} yields stronger fringe modulation, while larger w_{eff} leads to reduced visibility and fringe washout. The red vertical line marks $x = 0$, and the dashed line indicates the horizontal centerline used for the 1D profiles. All panels share the same linear color scale in expected detector counts per pixel.

positions remain aligned with the coherent reference, while increasing w_{eff} progressively fills the interference minima and suppresses higher-order oscillations. Under higher-coherence conditions, the profiles closely follow the coherent reference and retain strong peak-to-valley modulation across multiple fringe periods. In contrast, lower-coherence cases exhibit reduced interference contrast and approach a weakly modulated envelope-like distribution, resulting in significantly lower Michelson visibility (Section 3.1).

The parameter-specific comparisons follow the same trends identified in Fig. 3. Increasing the source size w [Fig. 4(a)] or pinhole diameter D [Fig. 4(d)] produces the strongest global reduction in modulation depth. Increasing the source–pinhole distance S [Fig. 4(b)] improves modulation through tighter angular filtering, whereas decreasing the pinhole–slit distance R [Fig. 4(c)] most effectively restores fringe contrast via near-field propagation that enhances mutual coherence at the slit separation. These results further confirm that detector fringe visibility is primarily governed by the effective source size w_{eff}, which serves as a convenient single-parameter descriptor of transverse coherence across different geometric configurations.

Figure 5 isolates the effect of longitudinal coherence by varying the relative spectral bandwidth under identical geometric conditions (w=20 µm, S=4.7 m, D=3 µm, R=5 cm). The Gaussian relative bandwidth σ_{BW} is increased from 0.10% to 5.0%, allowing the progressive wash-out of outer interference fringes to be examined independently of transverse-coherence effects.

Optics EXPRESS

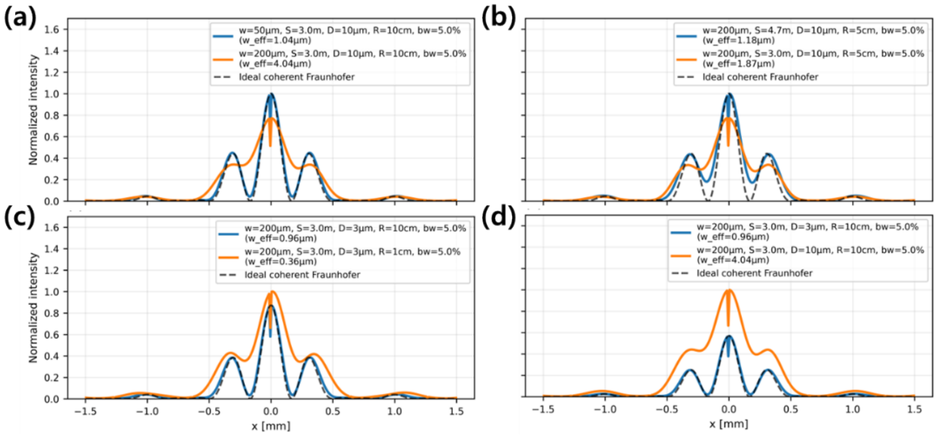

Fig. 4. Horizontal centerline intensity profiles extracted from the detector patterns in Fig. 3.Profiles are obtained along $z = 0$ by averaging five detector rows around the optical axis and plotting the normalized intensity as a function of detector coordinate x. Panels (a)–(d) correspond to the parameter variations in Fig. 3: (a) source size w, (b) source-to-pinhole distance S, (c) pinhole-to-slit distance R, and (d) pinhole diameter D. Increasing the effective source size w_{eff} progressively fills interference minima and suppresses higher-order oscillations, illustrating the loss of fringe visibility under reduced transverse coherence.

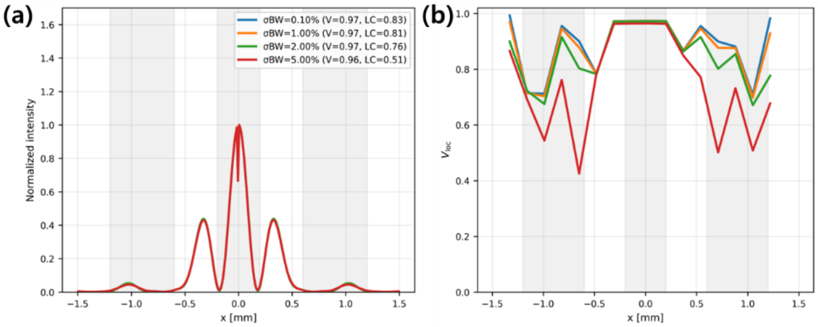

Fig. 5. Effect of spectral bandwidth on longitudinal coherence and outer-fringe contrast.(a) Normalized centerline intensity profiles for different relative bandwidths ($\sigma_{\mathrm{BW}} = 0.10\%, 1\%, 2\%, 5\%$) under identical geometric conditions ($w = 20\,\mu$m, $S = 4.70$ m, $D = 3.0\,\mu$m, $R = 5.0$ cm). The profiles are normalized to enable direct comparison of fringe modulation. Increasing bandwidth has little effect on the fringe spacing or the central fringe packet. (b) Local fringe visibility $V_{\mathrm{loc}}(x)$ evaluated using a sliding window approximately one fringe period wide. The shaded regions indicate the central and outer evaluation zones defined in this work. While the central visibility remains close to unity for all bandwidths, the outer-region visibility decreases systematically with increasing bandwidth, illustrating the progressive wash-out of outer fringes due to limited longitudinal coherence.

The centerline profiles in Fig. 5(a) are normalized for direct comparison. Even as the bandwidth increases, the fringe spacing and the overall structure of the central fringe packet remain nearly unchanged, and the global Michelson visibility remains high ($V \approx 0.96$–0.97). This indicates that the conventional global visibility metric alone is insufficient to distinguish bandwidth-induced fringe degradation.

A more sensitive measure is obtained by evaluating the local visibility $V_{\mathrm{loc}}(x)$ using a sliding window approximately one fringe period wide. The resulting distributions are shown in Fig. 5(b). In contrast to the global metric, the local visibility reveals that the effect of increasing bandwidth first appears at larger $|x|$, while the central region remains nearly unaffected. The shaded regions in the figure indicate the evaluation zones defined in this work (central and outer regions). In the central region, V_{loc} remains close to unity for all bandwidths, whereas in the outer region it decreases systematically with increasing σ_{BW}.

Consequently, the relative contrast metric LC_{ratio} (Eq (15)) decreases from 0.83 (0.10%) to 0.51 (5%), indicating that at σ_{BW}=5% the outer-fringe contrast is reduced to roughly half of the central contrast.

This behavior reflects the characteristic longitudinal-coherence limit: as the bandwidth increases, spectral averaging preferentially suppresses interference terms associated with larger optical path differences, leading to earlier degradation of outer fringes. For this reason, the present design framework does not rely solely on the global visibility V as a feasibility criterion. Instead, the outer-fringe preservation metric LC_{ratio} is included as an additional constraint to prevent solutions in which strong central fringes remain visible while outer fringes within the ROI are substantially degraded.

4.2. Coherence–flux trade-off and inverse-design maps

The coherence–flux trade-off can be visualized through inverse-design maps that identify operating points maximizing the FOM (Eq. (9)). Figure 6 summarizes these maps for two representative parameter spaces.

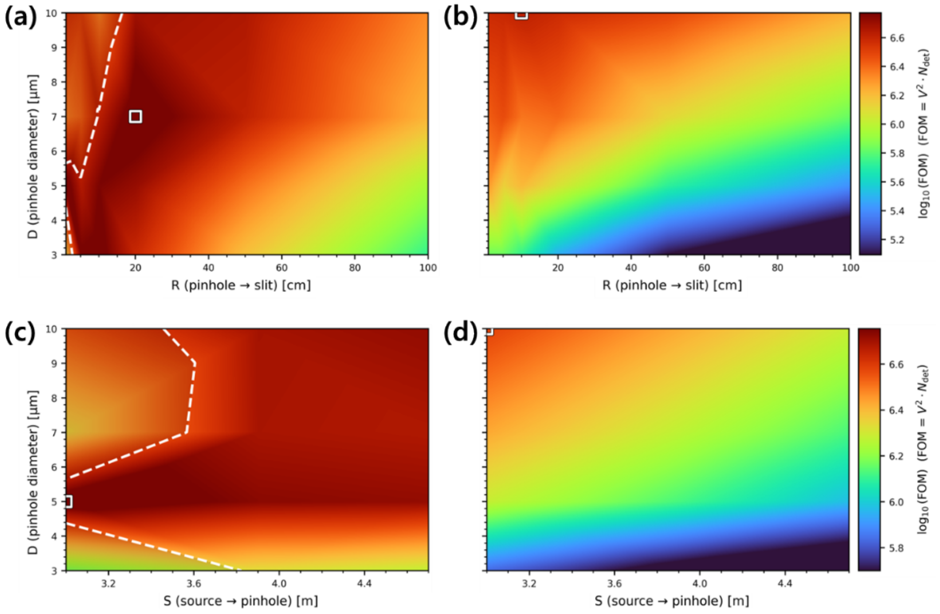

Fig. 6. Inverse-design maps illustrating the coherence–flux trade-off. The color scale shows $\log_{10}(\mathrm{FOM})$, where $\mathrm{FOM} = V^2 N_{\mathrm{det}}$. The white dashed contour denotes the feasibility boundary imposed by the visibility constraint (Michelson $V \geq 0.5$), and square markers indicate the optimal design within the feasible region. (a,b) Inverse-design maps in the $(R|D)$ plane at fixed S=3 m for (a) $w = 200\,\mu$m and (b) $w = 50\,\mu$m. (c,d) Inverse-design maps in the $(S|D)$ plane at fixed R=1 cm for (c) $w = 200\,\mu$m and (d) $w = 50\,\mu$m.

Figures 6(a) and (b) show inverse-design maps in the (R, D) plane at fixed S=3 m. The colormap represents $\log_{10}$(FOM), and the white dashed contour denotes the feasibility boundary defined by the visibility constraint $V \geq 0.5$. For the larger source (w=200 µm, Fig. 6(a)), the visibility requirement truncates the high-throughput region at small R and large D. Increasing the pinhole diameter enhances photon throughput but broadens the pinhole-plane angular spectrum, thereby reducing mutual coherence at the slit separation. The optimal design therefore occurs at an intermediate operating point (R≈20 cm, D≈7 µm), where photon throughput and fringe contrast are balanced.

For the smaller source (w=50 µm, Fig. 6(b)), the visibility threshold is satisfied across the scanned domain. The design becomes primarily flux-limited, and the FOM increases toward larger D and smaller R, shifting the optimum toward the most transmissive geometry.

Figures 6(c) and (d) provide a complementary inverse-design view in the (S, D) plane at fixed R=1 cm, illustrating how pinhole acceptance controlled by the source–pinhole distance S and the pinhole diameter D mediates the contrast–throughput balance. For the larger source (w=200 µm, Fig. 6(c)), the visibility constraint again restricts the accessible parameter space, particularly at shorter S where increasing pinhole diameter rapidly degrades transverse coherence. The FOM therefore forms a ridge at moderate aperture size, and the optimum lies near S≈3 m and D≈5 µm. In contrast, for the smaller source (w=50 µm, Fig. 6(d)), the feasibility boundary does not appear within the plotted domain, and the map is dominated by photon throughput, favoring the largest practical pinhole diameter.

Taken together, these maps reveal two distinct operating regimes. For larger sources the design is visibility-limited, and the optimum lies within a restricted feasible region defined by the coherence constraint. For smaller sources the system operates in a throughput-limited regime, where performance improves monotonically with increased photon acceptance.

4.3. Anchoring simulated photon statistics to experimental benchmarks

Feasibility in a YDS geometry is ultimately limited by photon statistics. To place the simulated detector signals on an experimentally meaningful scale, the absolute photon flux of the hybrid SHADOW3–WOFRY workflow was anchored to a published LMJ benchmark [7]. A single global calibration factor was applied to the SHADOW3-derived pinhole-transmitted ray weights such that the reference condition reproduces a transmitted flux of 5×10^3 photons/s through a D=5 µm pinhole. This normalization was then used for the entire parameter sweep. In addition, photon flux was scaled proportionally with the assumed Gaussian relative bandwidth σ_{BW}, allowing detector-level counts N_{det} and FOM values to be expressed in absolute photon units.

The consistency of this calibration is illustrated in Fig. 7(a), which plots the calibrated pinhole-transmitted photon flux as a function of pinhole diameter under the reference geometry (w=20 µm, S=3.9 m). By construction, the curve intersects the literature benchmark at D=5 µm. The model then predicts a monotonic increase in transmitted flux for larger apertures, reaching approximately 10^4 photons/s at D=7 µm and ~3×10^4 photons/s at D=10 µm. This provides a direct mapping between geometric design parameters and experimentally achievable photon throughput.

Using the same anchored normalization, Fig. 7(b) converts the simulated detector flux of a representative optimal design (w=200 µm, S=3 m, D=7 µm, R=20 cm, σ_{BW}=5%) into accumulated photons as a function of exposure time (assuming detector quantum efficiency QE = 1). The linear trends on the log–log axes reflect the expected scaling $N \propto t$. The calibrated model predicts that the detector-region photon budget reaches $\sim 10^8$ photons within approximately 10 s and $\sim 10^9$ photons within $\sim 10^2$ s. These values indicate that the inverse-designed operating points identified in Section 4.2 correspond to practical exposure times for laboratory experiments when the photon statistics are anchored to realistic source performance. This experimentally

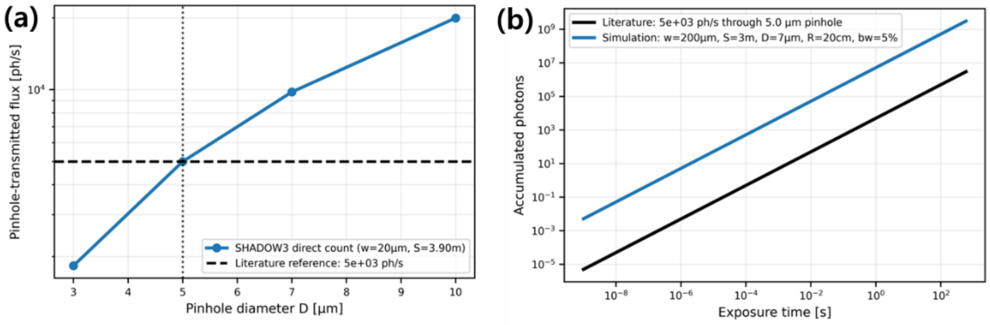

Fig. 7. Experimental anchoring of photon statistics. (a) Calibrated pinhole-transmitted photon flux as a function of pinhole diameter D obtained from SHADOW3 for the reference condition ($w = 20\,\mu$m, $S = 3.9\,$m). The global calibration factor is chosen such that the $D = 5\,\mu$m point (vertical dotted line) matches the benchmark flux (horizontal dashed line), enabling absolute photon budgets to be estimated across the design parameter sweep. (b) Accumulated photon counts in the detector ROI as a function of exposure time (log–log scale). The blue line shows the simulated photon accumulation for a representative optimal geometry ($w = 200\,\mu$m, $S = 3\,$m, $D = 7\,\mu$m, $R = 20\,$cm, $\sigma_{\mathrm{BW}} = 5\%$; QE = 1). The black line represents the literature benchmark corresponding to a flux of 5×10^3 photons/s through a $D = 5\,\mu$m pinhole.

anchored calibration therefore bridges the gap between simulation-based inverse design and realistic laboratory photon statistics.

5. Discussion

This work provides a detector-level and experimentally anchored framework for designing hard-X-ray YDS measurements with compact laboratory sources. By defining partial coherence at the pinhole plane using the pinhole-filtered angular spectrum from SHADOW3 and propagating a weighted angular-tilt ensemble through Fresnel (pinhole to slit) and Fraunhofer (slit to detector) operators in WOFRY, the workflow directly maps source and geometry choices to detector observables. In addition to detector images, the pipeline yields Michelson visibility, ROI photon budgets, and inverse-design maps, enabling feasibility to be assessed under coupled coherence–flux constraints rather than under coherence or throughput alone. This coupling is captured by the practical FOM and by feasibility boundaries imposed by a minimum visibility requirement and a longitudinal wash-out constraint.

5.1. Transverse coherence knobs and an effective single-parameter descriptor

Across the transverse-coherence knobs (w, S, R, D), the detector patterns and lineouts demonstrate a common mechanism: each knob primarily reshapes the pinhole-filtered angular distribution, thereby changing the mutual coherence delivered to the slit separation. In this sense, the Gaussian-equivalent effective source size w_{eff} provides a useful single-parameter descriptor of the slit-plane coherence state. Smaller w_{eff} corresponds to deeper interference minima and more persistent higher-order oscillations, whereas larger w_{eff} progressively fills the minima and suppresses modulation. The inverse-design maps further reveal two operating regimes. For larger sources, the design is visibility-limited: increasing pinhole acceptance (larger D) and/or operating too compactly (small R and/or S) increases throughput but can broaden the transmitted angular spectrum enough to violate the visibility threshold. For smaller sources, the visibility constraint is non-limiting over the scanned domain and performance becomes primarily throughput-limited, improving monotonically with photon acceptance.

The sharp falls near $x \approx 0$ in the line profiles in Fig. 4 are a numerical binning artifact rather than a physical coherence effect. In the current detector mapping, $x = 0$ falls on a pixel boundary (even number of pixels), and the energy-conserving binning convention assigns edge samples to one side, producing a one-pixel discontinuity across the origin. This can be removed by centering the origin on a pixel (odd number of pixels or a half-pixel shift), or by modifying the binning routine to split edge hits across adjacent bins. Because the visibility estimator is evaluated over windows spanning many pixels after envelope detrending, this single-bin artifact has negligible impact on the extracted visibility or on the inverse-design trends.

5.2. Longitudinal coherence and outer-fringe preservation

The bandwidth sweep highlights why a single global visibility number can be insufficient in compact laboratory geometries. Even when the global Michelson visibility remains high, increasing spectral width preferentially suppresses fringes at large $|x|$, where the effective optical path difference is larger, producing the characteristic outer-fringe wash-out associated with limited longitudinal coherence. The introduced metric $LC_{\text{ratio}} = V_{\text{outer}}/V_{\text{center}}$ explicitly targets this effect and excludes solutions that retain a high-contrast central packet but lose usable contrast in the outer region used for ROI-based statistics. Practically, preserving outer fringes improves the robustness of visibility estimation and reduces bias when coherence is inferred from detector data.

5.3. Anchored photon budgets and experimental feasibility

A common limitation of wave-optics design studies is that relative intensities are reported without establishing whether the predicted operating points correspond to realistic acquisition times. Here, anchoring the SHADOW3 pinhole-transmitted flux to a published LMJ benchmark provides an absolute photon scale for the full sweep, allowing N_{det}, FOM, and exposure-time requirements to be interpreted in laboratory units. Under this normalization, representative inverse-designed geometries that satisfy both visibility and wash-out constraints correspond to practical exposure times (seconds to minutes, depending on geometry and bandwidth). This anchoring therefore bridges simulation-based inverse design and experimentally achievable photon statistics, making the maps directly actionable for experiment planning.

5.4. Limitations and outlook

Several modeling assumptions should be considered when translating these results to a specific experiment. First, the double slit is treated as an ideal opaque amplitude mask; finite thickness, partial transmission, edge rounding, and phase shifts in real absorber structures may modify throughput and fringe contrast. Second, detector effects beyond pixel integration (PSF/charge sharing, background, saturation) are not included, and QE is set to unity unless specified, so experimental SNR will depend on detector response and stray scattering. Third, the partial-coherence model represents the source as an incoherent mixture of angular tilt modes derived from a pinhole-filtered histogram; while physically transparent and computationally efficient, extensions to more general coherent-mode decompositions may be warranted for sources with strong position–angle correlations or non-Gaussian statistics.

Despite these limitations, the present framework already addresses the central practical question for laboratory YDS design: which combinations of filtering strength and propagation distances yield simultaneously measurable fringe contrast and sufficient photon statistics within realistic exposure times. Future work will incorporate measured LMJ spectra (including multi-line structure), realistic detector response, and slit-mask material absorption, and will validate selected operating points experimentally to close the loop between inverse design and laboratory implementation.

6. Conclusion

We developed an end-to-end, detector-level framework for designing hard-X-ray YDS experiments with compact laboratory sources, explicitly capturing the coherence–flux trade-off under realistic detector sampling and photon statistics. The workflow couples SHADOW3 ray tracing with WOFRY wave-optics propagation by defining partial coherence at the pinhole plane via the pinhole-filtered angular spectrum and representing the source as a weighted angular-tilt ensemble. This approach provides a direct and physically transparent mapping from source and geometry parameters to experimentally measurable detector quantities, including two-dimensional interference patterns, Michelson visibility, detector-ROI photon budgets, and a practical figure of merit based on contrast and photon counts.

Representative detector patterns and lineouts showed that the primary geometric knobs (w, S, R, D) act primarily by reshaping the pinhole-transmitted angular spectrum and therefore the slit-plane mutual coherence, which can be compactly summarized using the Gaussian-equivalent effective source size w_{eff}. Inverse-design maps revealed two distinct operating regimes. For larger effective sources (e.g., w=200 µm), the feasible design space is visibility-limited, and the optimal operating point occurs at intermediate pinhole acceptance where photon throughput and fringe contrast are balanced. For smaller sources ($w\approx 50$ µm), the visibility constraint is non-limiting across the scanned domain and performance becomes primarily throughput-limited.

Finally, we anchored the absolute photon scale by calibrating the pinhole-transmitted flux to a published LMJ benchmark. Under this calibration, representative inverse-designed operating points produce detector-ROI photon budgets of order 10^8 photons within ∼10 s and 10^9 photons within $\sim 10^2$ s, demonstrating that the predicted high-visibility operating points correspond to practical exposure times for laboratory experiments.

Overall, the proposed framework provides a quantitative and experimentally grounded guideline for selecting source filtering and propagation geometry in laboratory YDS measurements.

Funding. Electronics and Telecommunications Research Institute (24YB2210); National Research Foundation of Korea (RS-2023-00302330).

Acknowledgment. This work was supported by internal fund/grant of Electronics and Telecommunications Research Institute (24YB2210). This research was also supported by the National Research Foundation of Korea (NRF) funded by the Korea government (MSIT) (RS-2023-00302330).

Disclosures. The authors declare no conflicts of interest.

Data availability. The data underlying the figures in this paper are generated by numerical simulations and are reproducible using the publicly available code. All Python scripts used for the simulations, detector-level analysis, and inverse-design map generation are openly available through [19]. Additional derived data products can be obtained from the authors upon reasonable request.

References

1. F. Zernike, "The concept of degree of coherence and its application to optical problems," Physica **5**(8), 785–795 (1938).
2. F. Eisenhauer, J. D. Monnier, and O. Pfuhl, "Advances in optical/infrared interferometry," Annu. Rev. Astron. Astrophys. **61**(1), 237–285 (2023).
3. V. Kohn, I. Snigireva, and A. Snigirev, "Direct measurement of transverse coherence length of hard X rays from interference fringes," Phys. Rev. Lett. **85**(13), 2745–2748 (2000).
4. W. Leitenberger, S. M. Kuznetsov, and A. Snigirev, "Interferometric measurements with hard X-rays using a double slit," Opt. Commun. **191**(1-2), 91–96 (2001).
5. T. E. Gureyev, C. Hall, B. Arhatari, *et al.*, "Young's double-slit interference with single hard X-ray photons," Opt. Express **32**(11), 19294–19307 (2024).
6. R. Castle, N. Appathurai, N. Simonson, *et al.*, "Investigating the limits of hard X-ray coherence length measurement employing Young's double slit experiment," Sci. Rep. **15**(1), 18159 (2025).
7. D. J. Batey, A. M. Maiden, and J. M. Rodenburg, "X-ray ptychography with a laboratory source," Phys. Rev. Lett. **126**(19), 193902 (2021).

8. J. C. da Silva, C. Guilloud, O. Hignette, *et al.*, “Overcoming the challenges of high-energy X-ray ptychography,” J. Synchrotron Radiat. **26**(5), 1751–1762 (2019).
9. L. B. Gromann, F. De Marco, C. Holzner, *et al.*, “Low-dose phase-contrast imaging with high signal-to-noise ratio,” Biomed. Opt. Express **7**(2), 381–391 (2016).
10. M. Sánchez del Río, N. Canestrari, and F. Jiang, “SHADOW3: a new version of the synchrotron X-ray optics modelling package,” J. Synchrotron Radiat. **18**(5), 708–716 (2011).
11. L. Rebuffi and M. Sánchez del Río, “OASYS (OrAnge SYnchrotron Suite): an open-source graphical environment for x-ray virtual experiments,” Proc. SPIE **10388**, 103880S (2017).
12. L. Rebuffi and M. Sánchez del Río, “ShadowOui: a new visual environment for X-ray optics and synchrotron beamline simulations,” J. Synchrotron Radiat. **23**(6), 1357–1367 (2016).
13. J. W. Goodman, *Introduction to Fourier Optics*, 3rd ed. (Roberts and Company, 2005).
14. M. Born and E. Wolf, *Principles of Optics*, 7th ed. (Cambridge Univ. Press, 1999).
15. M. Sánchez del Río, R. Celestre, and J. Reyes-Herrera, “A fast and lightweight tool for partially coherent beamline simulations based on coherent mode decomposition,” J. Synchrotron Radiat. **29**(6), 1354–1367 (2022).
16. J. W. Goodman, *Statistical Optics* (Wiley, 1985).
17. D. P. Jackson, N. Ferris, and J. Pearson, “Subtleties with Young’s double-slit experiment: investigation of spatial coherence and fringe visibility,” Am. J. Phys. **86**(9), 683–689 (2018).
18. L. Mandel and E. Wolf, *Optical Coherence and Quantum Optics* (Cambridge Univ. Press, 1995).
19. S. Choi, "yds_pcoh: Young’s Double-Slit: partial-coherent mode," GitHub (2026), https://github.com/schoi127/yds_pcoh.